Phase Locking between Different Partial Waves in Atom-Ion Spin-Exchange Collisions

Tomas Sikorsky,[1,*] Masato Morita,[2] Ziv Meir,[1] Alexei A. Buchachenko,[3,4] Ruti Ben-shlomi,[1] Nitzan Akerman,[5] Edvardas Narevicius,[5] Timur V. Tscherbul,[2] and Roee Ozeri[1]

[1]*Department of Physics of Complex Systems, Weizmann Institute of Science, Rehovot 7610001, Israel*
[2]*Department of Physics, University of Nevada, Reno, Nevada 89557, USA*
[3]*Skolkovo Institute of Science and Technology, Skolkovo Innovation Center, Building 3, Moscow 143026, Russia*
[4]*Institute of Problems of Chemical Physics RAS, Chernogolovka, Moscow Region 142432, Russia*
[5]*Department of Chemical Physics, Weizmann Institute of Science, Rehovot 7610001, Israel*

(Received 17 June 2018; published 25 October 2018)

We present a joint experimental and theoretical study of spin dynamics of a single $^{88}Sr^+$ ion colliding with an ultracold cloud of Rb atoms in various hyperfine states. While spin exchange between the two species occurs after 9.1(6) Langevin collisions on average, spin relaxation of the Sr^+ ion Zeeman qubit occurs after 48(7) Langevin collisions, which is significantly slower than in previously studied systems due to a small second-order spin-orbit coupling. Furthermore, a reduction of the endothermic spin-exchange rate is observed as the magnetic field is increased. Interestingly, we find that while the phases acquired when colliding on the spin singlet and triplet potentials vary largely between different partial waves, the singlet-triplet phase difference, which determines the spin-exchange cross section, remains locked to a single value over a wide range of partial waves, which leads to quantum interference effects.

DOI: 10.1103/PhysRevLett.121.173402

In recent years, the research of atom-ion collisions has entered the ultracold regime. Since the first demonstrations [1,2], laser-cooled atom-ion hybrid systems have matured into a successful field of research [3] and many new phenomena have been observed. Examples include state and spin controlled charge-exchange reactions [4,5], molecule formation [6,7], the emergence of power-law energy distributions and nonequilibrium dynamics [8,9], bifurcation of ion energies [10], sympathetic and swap cooling [9,11], three-body reactions [12–14], as well as spin exchange and spin relaxation in atom-ion collisions [5,15,16].

Spin dynamics in atom-ion systems is particularly interesting. A single spin-1/2 ion immersed in a cloud of ultracold spin-polarized atoms realizes the model of a controllable qubit coupled to a well-defined and adjustable environment [17,18]. Such a system can, for example, be used to model spin impurities in the solid state [19]. Understanding and controlling atom-ion spin dynamics is also essential for applications such as generating atom-ion entanglement or quantum gates [20,21]. Previous experiments which investigated the spin dynamics of a single ion interacting with an ultracold gas used Yb^+/Rb [15], Yb^+/Li [16], and Sr^+/Rb mixtures [5].

Here, we present a joint experimental and theoretical study of the spin dynamics of a single Sr^+ Zeeman qubit immersed in a spin-polarized bath of Rb atoms at mK temperature. Similar to previous experimentally used species, both ^{87}Rb and $^{88}Sr^+$ have a single electron in the valence shell. We carried out our measurements with Rb prepared in different hyperfine spin states and at two different magnetic fields. We found that similar to other systems, spin dynamics is governed by the competition between spin-exchange (SE) and spin-relaxation (SR) processes. However, here, SR was found to be slow compared with the Langevin collision rate [$48(7)\tau_L$]. This makes the Sr^+/Rb mixture promising for studying spin-dependent interactions. We found quantitative agreement between experimental observation and quantum scattering coupled-channel calculations based on *ab initio* potentials. Furthermore, we found that while at mK temperature multiple partial waves ($\sim$15) contribute to the SE cross section, the phase difference acquired between the spin singlet and triplet incoming channels is the same for all partial waves involved.

This new effect, which we term partial-wave phase locking, leads to a dramatic sensitivity of the SE cross section to a variation of the singlet-triplet energy gap even in the multiple partial-wave regime. Similar sensitivity has been observed in Ref. [16] and recent theoretical work has explored related effects in cold ion-atom and atom-atom collisions [22]. We show that the physical origin of partial-wave phase locking is the short-range nature of the spin-exchange interaction, which makes it independent of the orbital angular momentum of the collision complex that dominates long-range dynamics. This implies that analogous to resonant charge exchange [23,24], SE collision dynamics over a wide range of collision energies can be completely characterized by three parameters: the singlet and triplet scattering lengths and the atomic polarizability. Our results open up the possibility to efficiently control

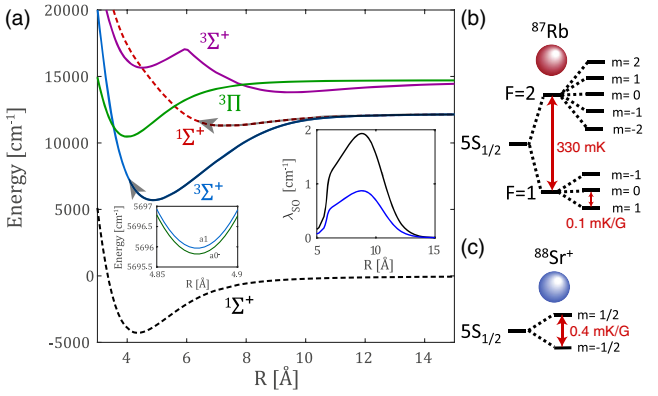

FIG. 1. (a) Relevant potential energy curves (PECs) of the $(RbSr)^+$ complex [43]. Left inset shows the splitting of the $^3\Sigma^+$ state into $a0^-$ and $a1$ components. Right inset shows the $\lambda_{SO}(R)$, the *ab initio* (black), and scaled (blue). (b),(c) Level structure of the $^{88}Sr^+$ and the ^{87}Rb ground states.

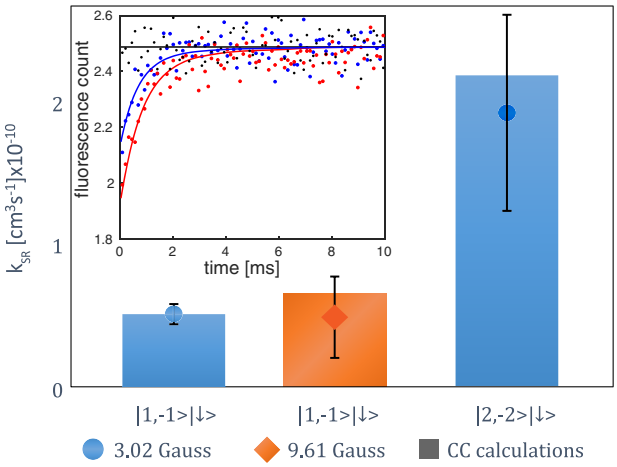

FIG. 2. Experimental spin-relaxation rate constants (k_{SR}) for various initial states and magnetic fields: $|1,-1\rangle_{Rb} \otimes |\downarrow\rangle_{Sr^+} \rightarrow |\text{all}\rangle_{Rb} \otimes |\uparrow\rangle_{Sr^+}$ and $|2,-2\rangle_{Rb} \otimes |\downarrow\rangle_{Sr^+} \rightarrow |F=1\rangle_{Rb} \otimes |\text{all}\rangle_{Sr^+}$. Bars represent the rate constants obtained from coupled-channel (CC) calculated cross sections convolved with a corresponding energy distribution. Inset shows Sr^+ ion fluorescence during Doppler cooling after 500 ms interaction time with $|2,-2\rangle$ (blue), $|2,0\rangle$ (red), and $|1,-1\rangle$ (black) Rb atoms. We extract the $|2,-2\rangle|\downarrow\rangle$ SR rate constant from a single parameter fit of the ion fluorescence curve and the $|1,-1\rangle|\downarrow\rangle$ SR rate constant from the electron-shelving measurements (see Fig. 3).

binary spin-exchange collisions in hot atomic and molecular gases by varying the singlet-triplet energy gap or the reduced mass of the collision complex. As an illustration, we predict a substantial (threefold) isotope effect for SE Sr^+-Rb collisions in the multiple partial-wave regime, which should be easily observable in near-future experiments.

In our experiment [25], a single Sr^+ ion is trapped in a linear Paul trap, ground state cooled to $\sim 40\ \mu K$ and spin polarized to a state either parallel ($m = 1/2$) $|\uparrow\rangle_{Sr^+}$ or antiparallel ($m = -1/2$) $|\downarrow\rangle_{Sr^+}$ to the magnetic field. Rb atoms are trapped in an optical trap, evaporatively cooled to $\sim 3\ \mu K$, and prepared in one of the spin states of the hyperfine manifold $|F, m_F\rangle$ of the electronic ground state Fig. 1(b). Interactions between the ion and the Rb cloud are initiated by moving the optical trap to overlap with the trapped ion. After various interaction times, the atoms are released from the trap, and the ion spin projection along the quantization axis is measured using electron shelving on an optical clock transition, followed by state-selective fluorescence [26,42].

First, we polarize our ion and atoms to the $|2,-2\rangle_{Rb} \otimes |\downarrow\rangle_{Sr^+}$ "stretched" state. This state belongs to the triplet manifold only and is therefore fully protected against SE. Here, any spin dynamics we observe is solely due to SR processes.

We use ion thermometry to extract the SR rate for the $|2,-2\rangle_{Rb} \otimes |\downarrow\rangle_{Sr^+}$ initial state. Since most spin-relaxation channels from $|2,-2\rangle_{Rb} \otimes |\downarrow\rangle_{Sr^+}$ lead Rb atoms to the $F = 1$ manifold, 328 mK of energy is released in the process. This energy release heats the ion and leads to a higher steady-state temperature which we detect using Doppler cooling thermometry. From the fluorescence recooling curve (blue points in the inset of Fig. 2), we can extract the energy distribution of the ion at steady state [44]. Through a comparison with a molecular dynamics simulation, the probability that hyperfine energy is released in a collision p_{HF} is extracted [26].

Our data indicate $p_{HF} = 0.079 \pm 0.028$, which translates to a hyperfine energy-release rate of once every $13(5)\tau_L$, shown in Fig. 2. Furthermore, when initializing Rb in the $|2,0\rangle_{Rb}$ state, we get a higher steady-state temperature (red points in the inset of Fig. 2), consistent with SE processes adding to the hyperfine energy-release rate.

The increased ion temperature makes direct ion spin measurements using electron-shelving techniques difficult [26], as the ion is quickly heated out of the Lamb-Dicke regime. We, therefore, turn to measuring spin dynamics when Rb is initialized in the $F = 1$ hyperfine ground manifold. We start by initializing Rb in the $|1,-1\rangle_{Rb}$ state. Here, we expect both SE and SR processes to play a role. When initializing Sr^+ in the $|\uparrow\rangle_{Sr^+}$ state, SE flips its spin to $|\downarrow\rangle_{Sr^+}$. However, when initializing in the $|\downarrow\rangle_{Sr^+}$ state, SE transfers Rb to the $F = 2$ hyperfine manifold. This process is energetically suppressed due to the 328 mK hyperfine energy gap. This asymmetry in SE collisions with Rb tends to polarize the ion spin to align with that of the atoms. An example of such a spin dynamics is shown in the inset of Fig. 3. The steady-state polarization of the ion spin is determined by the ratio of SE to SR rates. We extracted both rates by comparing the measured Sr^+ ion spin dynamics to rate equations [26].

In another measurement, we prepared Rb atoms in the $|1,0\rangle$ state with ions in either $|\uparrow\rangle$ or $|\downarrow\rangle$. Here, SE can work both ways: $|1,0\rangle_{Rb} \otimes |\uparrow\rangle_{Sr^+} \rightarrow |1,1\rangle_{Rb} \otimes |\downarrow\rangle_{Sr^+}$ and

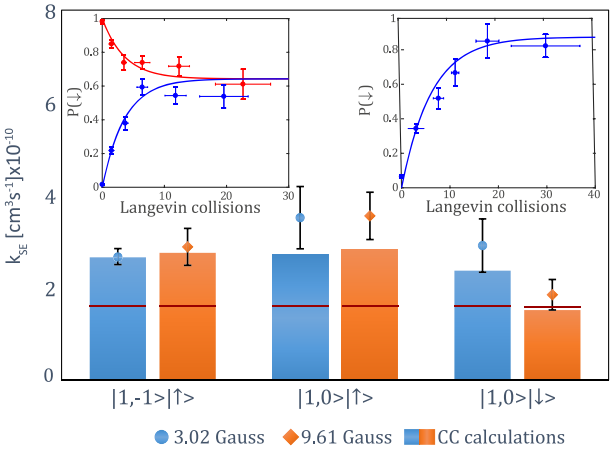

FIG. 3. Experimental spin-exchange rate constants (k_{SE}) for various initial states and magnetic fields. Bars represent the rate constants obtained from CC calculated cross sections convolved with a Tsallis energy distribution. Red line shows the RPA results showing a clear disagreement with most of our measured rates. Insets show an example of the raw experimental data that were used to extract the rate constant. The left inset shows the evolution of the ion spin state prepared in either the $|\uparrow\rangle_{Sr^+}$ or $|\downarrow\rangle_{Sr^+}$ state colliding with atoms in the $|1,0\rangle_{Rb}$ state. Right inset shows an ion initialized in the $|\uparrow\rangle$ state colliding with atoms in $|1,-1\rangle_{Rb}$. Both insets are for $B = 9.61$ G. The Langevin collision rate is $\Gamma \approx 1$ kHz.

$|1,0\rangle_{Rb} \otimes |\downarrow\rangle_{Sr^+} \rightarrow |1,-1\rangle_{Rb} \otimes |\uparrow\rangle_{Sr^+}$. The evolution of the ions' spin for both initial states is shown in the inset of Fig. 3. As seen, the steady-state polarization of the ion spin in this case is 0.64(1). The deviation from the expected value of 0.5 is due to small imbalance between the endo- and exothermic SE rates (see Fig. 3).

To theoretically explore SE collisions, we performed scattering calculations at various levels of sophistication, ranging from random-phase approximation (RPA), degenerate internal states approximation (DISA), to accurate CC calculations.

We begin with an expression of the SE cross section in the DISA [45–47], which assumes the degeneracy of internal states of Rb-Sr^+,

$$\sigma_{ex}^{DISA} = |\langle\Psi_i|\hat{\mathbf{S}}^{(Rb)} \cdot \hat{\mathbf{S}}^{(Sr^+)}|\Psi_f\rangle|^2 \frac{4\pi}{k^2} \sum_{l=0}^{\infty} (2l+1)\sin^2(\Delta\eta_l), \tag{1}$$

where $\hat{\mathbf{S}}$ is the electron spin operator, $\Psi_{i/f}$ describe the initial or final state of the Sr^+/Rb mixture, $\Delta\eta_l$ is the difference of the singlet (s) and triplet (t) scattering phase shifts $\eta_l^{s,t}$, k is the wave number, and l is the orbital angular momentum. According to Eq. (1), SE between Rb and Sr^+ can be thought of as an interference of the scattering wave functions on $V_{s,t}$: the singlet ($^1\Sigma^+$) and triplet ($^3\Sigma^+$) PECs in Fig. 1.

To obtain the scattering phase shifts, we carried out one-dimensional scattering calculations based on the calculated PECs [43] merged with the long-range form $V_{as}(R) = -C_4/R^4 - C_6/R^6$ using the C_n coefficients [48].

In the Langevin energy regime, Eq. (1) can be further approximated [$\sin^2(\Delta\eta_l) = 1/2$], which gives the RPA [49]

$$\sigma_{ex}^{RPA} = |\langle\Psi_i|\hat{\mathbf{S}}^{(Rb)} \cdot \hat{\mathbf{S}}^{(Sr^+)}|\Psi_f\rangle|^2 2\sigma_L, \tag{2}$$

where $\sigma_L = 2\pi\sqrt{C_4/E}$ is the Langevin cross section [50].

To solve the full ion-atom scattering problem including spin-orbit (SO) coupling, the hyperfine interaction, and an external magnetic field, we carry out CC calculations [26]. The second-order spin-orbit coupling coefficient λ_{SO} determines the strength of the effective spin-spin interaction between the electron spins of valence electrons of Rb and Sr^+. It was identified as the main source of spin non-conserving processes in the Yb^+/Rb system [15,26,51].

We calculated the SO coupling coefficient λ_{SO} as described in the Supplemental Material [26]. As shown in the inset of Fig. 1, its value is below 2 cm^{-1}, and in order to match the SR rate predicted by CC calculations to the measured value, we scaled it by a factor $c_{SO} = 0.45$. The scaling is necessary because quantitatively accurate calculations of λ_{SO} at such a small energy scale require extreme accuracy of the *ab initio* wave functions hardly attainable in practice.

We now compare our measured SE and SR rates to the results of the different calculations. The measured SR rate when initializing in $|1,-1\rangle_{Rb} \otimes |\downarrow\rangle_{Sr^+}$ of $48(7)\tau_L$ is shown in Fig. 2. The vertical bars in Fig. 2 show the calculated SR rate using the scaled λ_{SO} for both cases where Rb is initialized in the $|1,-1\rangle_{Rb}$ and $|2,-2\rangle_{Rb}$ states. As seen in the latter case, CC calculations reproduce the measured hyperfine-energy-release rate without additional adjustment of the λ_{SO} parameter. The fact that the SR is faster for $|2,-2\rangle_{Rb}$ atoms as compared to $|1,-1\rangle_{Rb}$ can be explained by the higher number of open relaxation channels for the $|2,-2\rangle_{Rb}|\downarrow\rangle$ state. Also, the matrix elements of the interaction involving the fully spin-stretched $|2,-2\rangle_{Rb}$ state are larger than those involving the $|1,-1\rangle_{Rb}$ state, leading to larger inelastic collision rates for the $F = 2$ hyperfine manifold of Rb.

The SE rate we extract from this measurement corresponds to the $|1,-1\rangle_{Rb} \otimes |\uparrow\rangle_{Sr^+} \rightarrow |1,0\rangle_{Rb} \otimes |\downarrow\rangle_{Sr^+}$ transition. Here, we observe SE once every $9.10(59)\tau_L$ on average. To match the CC calculated value obtained by convolving the CC cross sections with Tsallis energy distribution, we tune the singlet-triplet gap by scaling the singlet potential [26]. We find that the calculated SE cross sections are highly sensitive to this scaling, as shown in the inset of Fig. 4. We observe that the cross sections oscillate periodically with full contrast, which suggests coherent partial-wave phase locking as described below. A scaling factor of $c = 1.0005$ adequately matches our

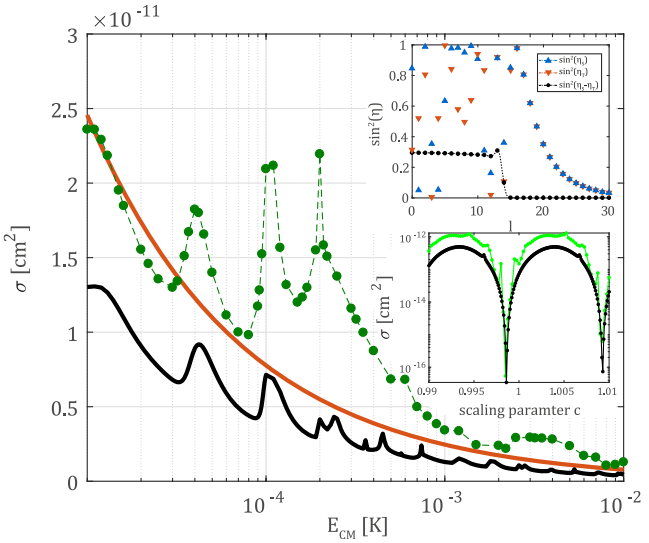

FIG. 4. $|1,-1\rangle_{\mathrm{Rb}} \otimes |\uparrow\rangle_{\mathrm{Sr}^+} \rightarrow |1,0\rangle_{\mathrm{Rb}} \otimes |\downarrow\rangle_{\mathrm{Sr}^+}$ spin-exchange cross section calculated at various levels of theoretical accuracy: RPA (red), DISA (black), and CC (green). The upper inset shows the difference of the scattering phase shifts $\sin^2(\Delta\eta_l)$ as a function of l obtained using the DISA at $E = 1$ mK. The individual scattering phase shifts on the singlet and triplet PECs $\sin^2(\eta_l^s)$ and $\sin^2(\eta_l^t)$ are shown by the blue and red filled circles, respectively. The lower inset shows the spin-exchange cross section at $E = 1$ mK as a function of the scaling parameter c, where the black line is for DISA, and the green line is the CC.

experimental result to CC theory. The scaled singlet potential is used throughout this Letter [26].

We next analyze the case of Rb atoms prepared in the $|1,0\rangle$ state. Because here SE and SR are experimentally indistinguishable, we assumed the same SR rates as for $|1,-1\rangle_{\mathrm{Rb}}$. The calculated SE rates agree with experimental rates (Fig. 3), which justifies our initial parametrization of the $\mathrm{Sr}^+/\mathrm{Rb}$ PEC.

As seen in Fig. 3, both theory and experiment indicate that for the increased magnetic field, a difference between the endo- and exoenergetic SE cross sections emerges. This is due to the Zeeman energetic barrier of 0.2 mK G^{-1}, which increases with the magnetic field. Because of energy conservation, increasing the magnetic field suppresses the SE cross section at different energies [26]. This demonstrates that magnetic field provides additional control over SE collisions.

To gain physical insight into the mechanism of SE collisions, we compare in Fig. 4 the CC results at $B = 3.02$ G with those obtained using the DISA and RPA. In all calculations, the cross sections scale as $\sigma \propto \sqrt{1/E}$, which confirms that spin exchange is a Langevin process [50,52,53]. We observe significant deviations of the results between the CC and DISA, which comes from neglecting the hyperfine interaction in the DISA. In particular, the interchannel coupling effect with the closed channels in the $F = 2$ manifold of Rb is significant [26]. On the other hand, the DISA cross section correctly shows the positions of a series of shape resonances because those are determined by the shape of PECs rather than the interchannel coupling. In the RPA, the resultant cross section is systematically larger than the DISA cross section, which implies a dependence of the cross section on the details of the PECs and a correlation between the difference of scattering phase shifts $\Delta\eta_l$ in different partial waves [Eq. (1)]. In what follows, we focus on these points.

A remarkable result, which was also recently observed in Ref. [16] and is apparent in the lower inset of Fig. 4 is the extreme sensitivity of SE cross section to the potential scaling parameter c both with CC and DISA [26]. This is unexpected, given that in the multiple partial wave regime, one would expect random variations of $\sin^2(\Delta\eta_l)$ with l in Eq. (1) and the lack of sensitivity of scattering cross sections to the PECs. To gain further insight, in Fig. 4, we plot the contributions $\sin^2(\eta_l^{s,t})$ from the individual phase shifts on the singlet and triplet PECs along with their difference $\sin^2(\Delta\eta_l)$. We observe that even though the $\sin^2(\eta_l^{s,t})$ for individual phase shifts change rapidly with l, their difference $\sin^2(\Delta\eta_l)$ remains constant and drops to zero after the height of the centrifugal barrier exceeds the collision energy $l > (1/\hbar)(16\mu^2 C_4 E)^{1/4}$. The phase locking is responsible for the unexpected giant oscillations in SE cross sections with respect to the scaling parameter c.

To elucidate the origin of partial-wave phase locking, we evaluate the scattering phase shift using the WKB approximation [54]

$$\eta_l^{s,t} = \int_{R_0}^{\infty} \sqrt{k^2 - \frac{(l+1/2)^2}{R^2} - U_{s,t}(R)}\, dR - \int_{R_0'}^{\infty} \sqrt{k^2 - \frac{(l+1/2)^2}{R^2}}\, dR, \tag{3}$$

where $k^2 = 2\mu E$, $U_{s,t}(R) = 2\mu V_{s,t}(R)$, and R_0 and R_0' are the classical turning points in the presence and in the absence of the potential. Separating the integration range in Eq. (3) into the short-range and long-range parts, we define the short-range phase shift $\eta_l^{s,t,\mathrm{SR}} = \int_{R_0}^{R_{\mathrm{mid}}} \sqrt{\cdots}\, dR - \int_{R_0'}^{R_{\mathrm{mid}}} \sqrt{\cdots}\, dR$ and the long-range phase shift $\eta_l^{s,t,\mathrm{LR}} = \int_{R_{\mathrm{mid}}}^{\infty} \sqrt{\cdots}\, dR - \int_{R_{\mathrm{mid}}}^{\infty} \sqrt{\cdots}\, dR$, with $R_{\mathrm{mid}} = 30 a_0$. Since $V_s(R) \simeq V_t(R)$ at long range, $\eta_l^{s,\mathrm{LR}} \simeq \eta_l^{t,\mathrm{LR}}$ as illustrated in Fig. 5. Thus, $\Delta\eta_l$ is determined entirely by the difference of the short-range phase shifts as $\Delta\eta_l \simeq \eta_l^{s,\mathrm{SR}} - \eta_l^{t,\mathrm{SR}}$.

The value of R_{mid} was chosen such that the spin-exchange interaction is negligible for $R > R_{\mathrm{mid}}$ and the interaction potentials $V_{s,t}(R < R_{\mathrm{mid}})$ are much larger than the centrifugal energy. In Fig. 5, we observe that the individual short-range phase shifts as well as their difference depend on l only very weakly due to the small magnitude of the centrifugal potential compared with the

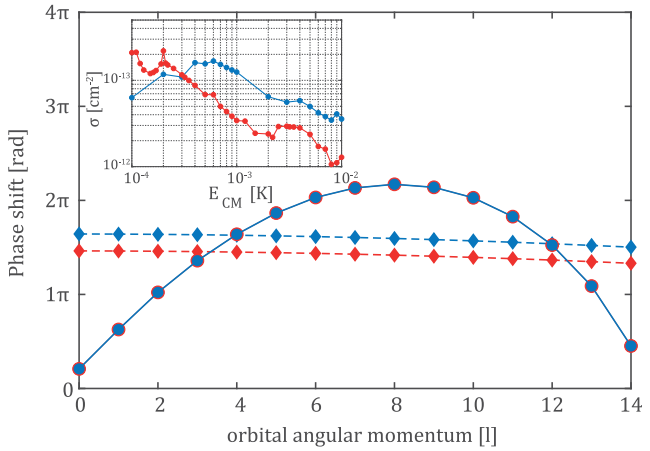

FIG. 5. Short- (diamonds) and long- (circles) range phase shifts as a function of l for the scattering wave functions on the singlet (red) and triplet (blue) potential energy curves at $E = 1$ mK with $R_{\mathrm{mid}} = 30a_0$. Modulus is 2π for short range and 4π for long range. Inset: Isotope dependence of the spin-exchange cross section with $^{88}Sr^+$ (red) and $^{86}Sr^+$ (blue) using CC calculations ($B = 3.02$ G).

potential well depth at short range. The physical origin of phase locking can thus be attributed to the short-range nature of the SE interaction and to the large potential well depth which renders short-range physics independent of l [55]. In other words, centrifugal forces play an important role only at atom-ion separations at which spin-exchange interaction is negligible. A sensitivity to the singlet-triplet gap could lead to a significant difference in the SE rate between different isotopes. The inset of Fig. 5 shows a comparison between the calculated SE cross sections of $^{86}Sr^+$ and $^{88}Sr^+$ colliding with ^{87}Rb atoms indeed predicting a threefold ratio between the cross sections over a wide range of energies.

In conclusion, we have studied experimentally and theoretically the spin dynamics of a single $^{88}Sr^+$ ion immersed in a spin-polarized cloud of ^{87}Rb atoms. We have shown that for this mixture, spin dynamics is dominated by spin exchange while spin relaxation is suppressed due to weak spin-orbit coupling. Our measurements are in excellent agreement with theoretical calculations. Furthermore, by varying the ambient magnetic field, we have been able to control the rate of endothermic spin exchange. This ability, together with slow spin relaxation, suggests that working at high magnetic fields it would be possible to freeze spin populations in this particular mixture for a long time. Interestingly, we have found that at our collision energy, the collision cross section is largely independent of the partial wave involved, leading to coherent oscillation in the spin-exchange rate as atomic potentials are varied. A future measurement of the spin-exchange rate using a different isotope of the Sr ion, $^{86}Sr^+$, would verify this phase-locking effect.

We thank Olivier Dulieu and Lothar Ratschbacher for useful discussions. This work was supported by the Crown Photonics Center, ICore-Israeli Excellence Center Circle of Light, the Israeli Science Foundation, the U.S.-Israel Binational Science Foundation, and the European Research Council (consolidator Grant No. 616919-Ionology). The work at University of Nevada, Reno, was supported by National Science Foundation Grant No. PHY-1607610.

*tomas.sikorsky@weizmann.ac.il

[1] C. Zipkes, S. Palzer, C. Sias, and M. Kohl, Nature (London) **464**, 388 (2010).
[2] S. Schmid, A. Härter, and J. H. Denschlag, Phys. Rev. Lett. **105**, 133202 (2010).
[3] S. Willitsch, *Ion Traps for Tomorrow's Applications* (2014), pp. 255–268.
[4] L. Ratschbacher, C. Zipkes, C. Sias, and M. Köhl, Nat. Phys. **8**, 649 (2012).
[5] T. Sikorsky, Z. Meir, R. Ben-Shlomi, N. Akerman, and R. Ozeri, Nat. Commun. **9**, 920 (2018).
[6] F. H. J. Hall, M. Aymar, N. Bouloufa-Maafa, O. Dulieu, and S. Willitsch, Phys. Rev. Lett. **107**, 243202 (2011).
[7] J. Wolf, M. Deiß, A. Krükow, E. Tiemann, B. P. Ruzic, Y. Wang, J. P. Dincao, P. S. Julienne, and J. H. Denschlag, Science **358**, 921 (2017).
[8] Z. Meir, T. Sikorsky, R. Ben-shlomi, N. Akerman, Y. Dallal, and R. Ozeri, Phys. Rev. Lett. **117**, 243401 (2016).
[9] Z. Meir, M. Pinkas, T. Sikorsky, R. Ben-shlomi, N. Akerman, and R. Ozeri, Phys. Rev. Lett. **121**, 053402 (2018).
[10] S. J. Schowalter, A. J. Dunning, K. Chen, P. Puri, C. Schneider, and E. R. Hudson, Nat. Commun. **7**, 12448 (2016).
[11] K. Ravi, S. Lee, A. Sharma, G. Werth, and S. A. Rangwala, Nat. Commun. **3**, 1126 (2012).
[12] A. Härter, A. Krükow, A. Brunner, W. Schnitzler, S. Schmid, and J. H. Denschlag, Phys. Rev. Lett. **109**, 123201 (2012).
[13] A. Krükow, A. Mohammadi, A. Härter, J. H. Denschlag, J. Pérez-Ríos, and C. H. Greene, Phys. Rev. Lett. **116**, 193201 (2016).
[14] C. H. Greene, P. Giannakeas, and J. Pérez-Ríos, Rev. Mod. Phys. **89**, 035006 (2017).
[15] L. Ratschbacher, C. Sias, L. Carcagni, J. M. Silver, C. Zipkes, and M. Köhl, Phys. Rev. Lett. **110**, 160402 (2013).
[16] H. Fürst, T. Feldker, N. V. Ewald, J. Joger, M. Tomza, and R. Gerritsma, Phys. Rev. A **98**, 012713 (2018).
[17] A. J. Leggett, S. Chakravarty, A. T. Dorsey, M. P. Fisher, A. Garg, and W. Zwerger, Rev. Mod. Phys. **59**, 1 (1987).
[18] N. V. Prokof'ev and P. C. Stamp, Rep. Prog. Phys. **63**, 669 (2000).
[19] U. Bissbort, D. Cocks, A. Negretti, Z. Idziaszek, T. Calarco, F. Schmidt-Kaler, W. Hofstetter, and R. Gerritsma, Phys. Rev. Lett. **111**, 080501 (2013).
[20] T. Secker, R. Gerritsma, A. W. Glaetzle, and A. Negretti, Phys. Rev. A **94**, 013420 (2016).
[21] H. Doerk, Z. Idziaszek, and T. Calarco, Phys. Rev. A **81**, 012708 (2010).
[22] R. Côté and I. Simbotin, Phys. Rev. Lett. **121**, 173401 (2018).

[23] M. Li and B. Gao, Phys. Rev. A **86**, 012707 (2012).
[24] M. Li, L. You, and B. Gao, Phys. Rev. A **89**, 052704 (2014).
[25] Z. Meir, T. Sikorsky, R. Ben-shlomi, N. Akerman, M. Pinkas, Y. Dallal, and R. Ozeri, J. Mod. Opt. **65**, 501 (2018).
[26] See Supplemental Material at http://link.aps.org/supplemental/10.1103/PhysRevLett.121.173402, for a detailed description of the experimental apparatus, scattering calculation methods, rate equations, Tsallis energy distribution, spin-relaxation rate extracted using the simulation of hyperfine energy release and Doppler recooling thermometry, which includes Refs. [27–41].
[27] M. D. Gregoire, I. Hromada, W. F. Holmgren, R. Trubko, and A. D. Cronin, Phys. Rev. A **92**, 052513 (2015).
[28] M. Cetina, A. T. Grier, and V. Vuletić, Phys. Rev. Lett. **109**, 253201 (2012).
[29] C. Zipkes, L. Ratschbacher, C. Sias, and M. Kohl, New J. Phys. **13**, 053020 (2011).
[30] T. Sikorsky, Quantum control of inelastic processes in atom-ion systems, thesis, Weizmann Institute of Science, 2018, https://www.weizmann.ac.il/complex/ozeri/sites/complex.ozeri/files/uploads/tsthesis.pdf.
[31] Z. Idziaszek, T. Calarco, P. S. Julienne, and A. Simoni, Phys. Rev. A **79**, 010702 (2009).
[32] Z. Idziaszek, A. Simoni, T. Calarco, and P. S. Julienne, New J. Phys. **13**, 083005 (2011).
[33] F. H. Mies, C. J. Williams, P. S. Julienne, and M. Krauss, J. Res. Natl. Inst. Stand. Technol. **101**, 521 (1996).
[34] D. E. Manolopoulos, J. Chem. Phys. **85**, 6425 (1986).
[35] M. Tomza, C. P. Koch, and R. Moszynski, Phys. Rev. A **91**, 042706 (2015).
[36] A. O. G. Wallis and J. M. Hutson, Phys. Rev. Lett. **103**, 183201 (2009).
[37] C. L. Blackley, C. R. Le Sueur, J. M. Hutson, D. J. McCarron, M. P. Köppinger, H.-W. Cho, D. L. Jenkin, and S. L. Cornish, Phys. Rev. A **87**, 033611 (2013).
[38] D. A. Brue and J. M. Hutson, Phys. Rev. Lett. **108**, 043201 (2012).
[39] A. Berning, M. Schweizer, H.-J. Werner, P. J. Knowles, and P. Palmieri, Mol. Phys. **98**, 1823 (2000).
[40] H.-J. Werner, P. J. Knowles, G. Knizia, F. R. Manby, M. Schütz *et al.*, MOLPRO, version 2015.1, a package of *ab initio* programs, 2015.
[41] A. Kramida, Yu. Ralchenko, J. Reader, and the NIST ASD Team, NIST Atomic Spectra Database, version 5.5.2, 2015 https://physics.nist.gov/asd.
[42] A. Keselman, Y. Glickman, N. Akerman, S. Kotler, and R. Ozeri, New J. Phys. **13** (2011).
[43] M. Aymar, R. Guérout, and O. Dulieu, J. Chem. Phys. **135**, 064305 (2011).
[44] T. Sikorsky, Z. Meir, N. Akerman, R. Ben-shlomi, and R. Ozeri, Phys. Rev. A **96**, 012519 (2017).
[45] A. Dalgarno, Proc. R. Soc. A **262**, 132 (1961).
[46] A. Dalgarno and M. R. H. Rudge, Proc. R. Soc. A **286**, 519 (1965).
[47] B. J. Verhaar, J. M. V. A. Koelman, H. T. C. Stoof, O. J. Luiten, and S. B. Crampton, Phys. Rev. A **35**, 3825 (1987).
[48] J. Kaur, D. K. Nandy, B. Arora, and B. K. Sahoo, Phys. Rev. A **91**, 012705 (2015).
[49] R. D. Levine, *Molecular Reaction Dynamics* (Cambridge University Press, 2005), pp. 1–554, ISBN: 9780521842761.
[50] P. Langevin, Ann. Chim. Phys. **5**, 245 (1905).
[51] T. V. Tscherbul, P. Brumer, and A. A. Buchachenko, Phys. Rev. Lett. **117**, 143201 (2016).
[52] R. Côté and A. Dalgarno, Phys. Rev. A **62**, 012709 (2000).
[53] O. P. Makarov, R. Côté, H. Michels, and W. W. Smith, Phys. Rev. A **67**, 042705 (2003).
[54] R. E. Langer, Phys. Rev. **51**, 669 (1937).
[55] B. Gao, Phys. Rev. A **64**, 010701 (2001).